Transport properties of C and O in UN fuels

Thomas Schuler, Denise Adorno Lopes, Antoine Claisse, and Pär Olsson

Phys. Rev. B **95**, 094117 — Published 23 March 2017

DOI: 10.1103/PhysRevB.95.094117

Transport properties of C and O in UN fuels

Thomas Schuler*
Department of Materials Science and Engineering, University of Illinois, Urbana-Champaign, Illinois 61801, USA

Denise Adorno Lopes, Antoine Claisse, and Pär Olsson
Reactor physics, KTH - Royal Institute of Technology, Stockholm, Sweden
(Dated: February 28, 2017)

Uranium nitride fuel is considered for fast reactors (GEN-IV generation and space reactors) and for light water reactors as a high-density fuel option. Despite this large interest, there is a lack of information about its behavior for in-pile and out-of-pile conditions. From the present literature, it is known that C and O impurities have significant influence on the fuel performance. Here, we perform a systematic study of these impurities in the UN matrix using electronic-structure calculations of solute-defect interactions and microscopic jump frequencies. These quantities were calculated in the DFT+U approximation combined with the occupation matrix control scheme, to avoid convergence to metastable states for the $5f$ levels. The transport coefficients of the system were evaluated with the self-consistent mean-field theory. It is demonstrated that carbon and oxygen impurities have different diffusion properties in the UN matrix, with O atoms having a higher mobility, and C atoms showing a strong flux coupling anisotropy. The kinetic interplay between solutes and vacancies is expected to be the main cause for surface segregation, as incorporation energies show no strong thermodynamic segregation preference for (001)-surfaces compared with the bulk.

I. INTRODUCTION

UN is considered as one of the most promising fuels for fast nuclear reactors, Generation IV and space rectors[1–3]. Additionally, it has also been considered as a new high-density fuel option for commercial light water reactors, allowing for a longer fuel residence time in the reactor[4]. The increased cycle period leads to fewer refueling shut downs and is thus an economical driving force for nitride fuel implementation. The UN compound is an attractive fuel option due to the combination of high fissile nuclide density, higher thermal conductivity, and high melting point[5]. The combination of all these properties results in a significantly lower fuel centerline temperature and smaller pellet temperature gradient, resulting in larger safety margins for reactor operation.

However, the use of UN was limited in the early years due to technological problems such as high pyrophoricity of the powder in air, poor water/steam tolerance, high difficulty in sintering the powder to a densified compact, and need for use of N^{15} instead of the natural N^{14} [6–9]. The issue related to the nitrogen enrichment persists because it is necessary to have a N^{15} concentration greater than 90% to sufficiently increase the neutron economy, reduced by the high absorption cross-section of N^{14}. N^{15} is not available in large scale, and there are still economics issues regarding the process to obtain it[9]. Moreover, the high pyrophoricity in powder condition also causes serious problems to establish an industrial fabrication route[7]. Obtaining powder with oxygen content below 1500 ppm, required for fuel application, is even today something implemented only at the laboratory scale. However, the strong potential benefits of the fuel motivates continued research and development activities world-wide.

Due to these technological challenges, there is a significant lack of data about systems involving UN fuel. Yet, irradiation experiments have been conducted in fast and thermal reactors, from which thermal and radiation creep was measured as a function of temperature, burnup, and porosity[10,11]. From these results, it was demonstrated that the presence of carbon (C) and oxygen (O) impurities strongly increase the swelling, and can lead to carbonization of the inner surface of the cladding[11]. For this reason, the maximum amount of these impurities was set to 0.1-0.15 wt% for reliable operation of fuel elements[11]. Understanding the underlying mechanisms governing the diffusion and segregation of C and O in UN is thus highly motivated. However, there is currently no data for diffusion coefficients of C and O in the UN matrix, mainly due to experimental difficulties. Thus, modeling can play an important part in advancing the licensing process of the UN fuel and to guide dedicated experiments.

In recent years, density functional theory (DFT) and the DFT+U methods have been used to investigate the UN bulk properties. For instance, Modak *et al.*, investigated the electronic, vibrational elastic and structural properties of UN over pressure region of 0-100 GPa[12]; Gryaznov *et al.* studied the atomic, electronic and low temperature magnetic structure of UN[13]; Tao Bo *et al.* investigated the intrinsic point defects of barium, zirconium and xenon as well as the absorption of H_2O in (001) surface[14]; Bocharov *et al.*[15,16] investigated the basic properties of the surface and the incorporation of O atoms. The idea behind the DFT+U method is to treat the strong on-site Coulomb interaction of localized electrons, which is not correctly describe by LDA or GGA, with an additional energy term (Hubbard)[17]. However, it is known that this method may introduce metastable states[18] with no physical meaning. This issue was extensively investigated for the UN system by Claisse *et al.*[19],

where the occupation matrix control (OMC) scheme was used to avoid metastable states in this material[20]. Using the combination of DFT+U+OMC, the equilibrium properties of C and O in UN bulk were computed by Lopes *et al.*[21]. However, the influence of the interaction between impurity atoms and the vacancy on the long range diffusion has not been studied.

The self-consistent mean-field (SCMF) method allows to compute transport coefficients (which control the kinetic properties of the system) from atomic jump rates computed with DFT[22–28]. It uses a thermal average of a microscopic master equation to compute the deviation of the probability of each configuration (with respect to equilibrium) under a chemical potential gradient. The SCMF method provides a formal link between individual jump processes at the atomic scale and long range diffusion which is responsible for microstructure evolution. This method of growing interest has been applied to various crystal structures, various diffusion mechanisms, strained systems, and non-homogeneous driving forces[22–28].

In this work, the DFT+U+OMC and the SCMF method are applied to understand the mobility and long range diffusion of carbon and oxygen in the UN lattice. We first introduce the aforementioned methods in Sec. II. Then we present the energetic calculations (incorporation, binding and migration) in Sec. III A, followed by a detailed study of solute transport coefficients and migration mechanisms in Sec. III B. Finally solute segregation induced by irradiation is discussed in Sec. III C.

II. METHODS

A. Density-functional theory calculations

First-principles calculations in this work were performed using the plane-wave-based DFT method implemented in the Vienna ab initio simulation package (VASP)[29–31]. The eletronic exchange and correlation energies were calculated within the generalized gradient approximation in the Perdew-Burke-Ernzerhof formalism[32]. The valence electrons explicitly treated in the calculations were $6s^2 6p^6 6d^2 5f^2 7s^2$ for U; $2s^2 2p^2$ for C; $2s^2 2p^3$ for N; and $2s^2 2p^4$ for O and a cut-off energy of 600 eV was used. To handle correctly the strong correlation of the $5f$ electrons, the Liechtenstein implementation of the Hubbard correlation is used with U = 2.0 eV and J = 0.1 eV[19,33]. To avoid the convergence toward metastable states previously demonstrated for this system[19] the occupation matrix control scheme was also applied[20]. In a previous study, the localized spins on the uranium ions were shown to have antiferromagnetic (AFM) ordering[19], thus this is the spin ordering adopted in this work.

Calculations of the UN bulk structure were performed with two reference supercells composed of 32 and 108 uranium atoms (and as many nitrogen atoms), in a rocksalt structure, slightly orthorhombic (a=4.9005 Å, b=4.9722 Å and c=5.0352 Å) as reported in Ref. 21. The 32-atom supercell was used to calculate incorporation energies and the 108-atom supercell was used to compute binding and migration energies. The UN(001) surface structure, which is the most stable surface in UN[34], was modeled by a periodic slab (2×2) which consists of nine atomic monolayers, with a total of 72 uranium atoms and 72 nitrogen atoms. A vacuum of 20 Å along the surface normal direction was set in order to prevent interactions between periodic replicas of the slab. Brillouin zone integration was performed using $4\times4\times4$ and $2\times2\times2$ k-points grids for UN bulk structures (depending on the supercell size), and a $4\times4\times1$ k-points grid for UN(001) surfaces, all generated using the Monkhorst-Pack scheme[35]. Atomic relaxations were performed without symmetry constraints and the internal structural parameters were relaxed until the energy was converged to less than 10 meV per atom. All atoms and atomic layers were allowed to relax fully for the UN(001) surface system. The nudged elastic band (NEB) method[36,37] with the climbing image algorithm using 3 intermediate images was used to compute migration barriers. We investigated both binding and migration energies of C and O around a vacancy, with the solutes and point defects being located on the nitrogen sublattice only. The uranium sublattice was not considered in this study because C and O exhibit dynamical instability on these sites[21].

The binding energies displayed in Table II show that at 4NN (Nearest-Neighbor) distance, the solute-vacancy interaction is much smaller than at shorter distances, which gives an idea of the extent of these interactions. Because our supercells are more than twice this distance in each direction, we think that the interaction between supercell replicas should have little effect on binding and migration energies. For isolated solutes and vacancy we used the ANETO code[38] to compute the elastic interaction energy between supercell replicas; it is less than 8%, 4% and 10% of the formation energy, respectively for C, O and N-vacancy, which is acceptable. The thickness of the UN(001) surface slab geometries was chosen following the work by Bocharov[15,16], who showed that defect formation energies are converged for slabs thicker than five atomic layers.

We did not estimate the vacancy prefactor for each vacancy jump around the solutes because diffusion coefficients are not very sensitive to these quantities while the required computational effort is burdensome. A complete calculation of attempt frequency requires the computation of the full force-constant matrix. Approximate values of the force-constant matrix have often been used but the convergence of attempt frequency is not straightforward[25], such that one cannot estimate the accuracy of these approximations a priori. For 230 solutes divided among 7 solvents with various crystallographic structures, variation of individual mechanisms attempt frequencies with respect to the isolated vacancy jump are all within a factor of 0.13-2.04[39] such that kinetic correlations are almost entirely monitored by migration ener-

gies, except at high temperatures. Hence, it is likely that a complete calculation of attempt frequencies would only shift solute diffusion coefficients by at most one order of magnitude. For these reasons, we used the simple Debye frequency value (23,8 THz) for all attempt frequencies, as in previous work[40].

B. Transport coefficients framework

The self-consistent mean field method (SCMF) has seen growing interest and development in the last fifteen years[22–28]. For solute and point-defect diffusion, it provides a general link between the atomic scale (individual jump rates) and the macroscopic scale (transport coefficients). In the framework of the thermodynamics of irreversible processes, transport coefficients determine the magnitude and sign of species and defect fluxes in response to a thermodynamic driving force (chemical potential gradient)

$$\begin{pmatrix} J_V \\ J_S \end{pmatrix} = -\begin{pmatrix} L_{VV} & L_{VS} \\ L_{SV} & L_{SS} \end{pmatrix} \begin{pmatrix} \nabla\dfrac{\mu_V - \mu_N}{k_\mathrm{B}T} \\ \nabla\dfrac{\mu_S - \mu_N}{k_\mathrm{B}T} \end{pmatrix}. \quad (1)$$

Equation 1 is written for the system of interest in this paper: vacancies (V) and solutes (S = C, O) migrating on the N-sublattice of the UN rocksalt structure. J_V (J_S) is the flux of vacancies (resp. solutes) in a given crystallographic direction; $L_{\alpha\beta}$ denotes transport coefficients, which depend on the diffusion direction, because of AFM ordering; ∇ denotes the gradient operator projected along the diffusion direction; k_B is the Boltzmann constant; T is the temperature; μ_V and μ_S are the vacancy and solute chemical potentials, respectively. Using the Gibbs-Duhem relation[41], there are only two independent chemical potential, hence the subtraction of a reference chemical potential: the nitrogen (matrix atom) chemical potential. The SCMF technique has been described in details elsewhere[23,27]. Simplifying assumptions (diffusive transitions only, dilute limit) allow to compute the steady-state flux resulting from an imposed driving force, and it is then possible to identify transport coefficients using Eq. 1.

As in Ref. 42, the SCMF method is applied in an AFM face-centered cubic structure (N-sublattice of UN), which has the same symmetry as a face-centered tetragonal structure. Thus there are two diffusion directions to consider: the T-direction (tangential) which is parallel to spin planes in the AFM ordering, and the N-direction which is perpendicular to spin planes. The dilute limit hypothesis assumes that no cluster larger than VS pairs (S =C or O) affects transport coefficients, especially $V-V$ and $S-S$ interplay are not accounted for. The transport matrix in Eq. 1 is divided into cluster transport contributions, as introduced in Ref. 27:

$$\begin{aligned}\begin{pmatrix} L_{VV} & L_{VS} \\ L_{SV} & L_{SS} \end{pmatrix} &= [V]\,M\,(V)\begin{pmatrix} 1 & 0 \\ 0 & 0 \end{pmatrix} \\ &+ [VS]\,M\,(VS)\begin{pmatrix} 1 & 1 \\ 1 & 1 \end{pmatrix} \\ &+ [VS]\begin{pmatrix} AD_{VV}\,(VS) & AD_{VS}\,(VS) \\ AD_{SV}\,(VS) & AD_{SS}\,(VS) \end{pmatrix}, \end{aligned} \quad (2)$$

where $[\alpha]$ is the volumetric concentration of cluster α, either an isolated vacancy (V), an isolated solute atom (S) or a vacancy solute pair (VS). There is no contribution for isolated solute atoms because they only migrate through vacancy-mediated jumps. VS pairs have two contributions, because they can either migrate as a whole (which gives rise to the mobility contribution $M\,(VS)$) or associate and dissociate (which is included in the $AD\,(VS)$ terms). Note that the association of an isolated vacancy with an isolated solute is included in this contribution. Furthermore, detailed balance implies the equality between the association and dissociation contributions, which is the reason why they are grouped together. The transport coefficient associated with cluster α is thus generally written as

$$L_{\beta\gamma}(\alpha) = M(\alpha) + AD_{\beta\gamma}(\alpha), \quad (3)$$

where $\beta, \gamma \in \{V, S\}$.

The radiation-induced segregation phenomenon stems from the off-diagonal terms of the total transport matrix[43]. Equation 2 shows that without VS pairs there would be no flux coupling, and that the sign of the flux coupling depends on the association/dissociation term, the mobility contribution being always positive. We define two quantities that will be used to study out-of-equilibrium impurity segregation: the VS pair drag ratio $L_{VS}(VS)/L_{SS}(VS)$ and the flux ratio ϕ. The drag ratio is an intrinsic property of VS pairs, and characterizes the qualitative nature of vacancy-solute flux coupling: the drag effect occurs when the drag ratio is positive (both V and S flowing in the same direction) and the inverse Kirkendall effect occurs when the drag ratio is negative (V and S flow in opposite directions). The drag ratio alone is not sufficient to understand radiation-induced segregation, because we also need to account for the diffusion of matrix atoms with respect to impurity atoms. To this end, a flux ratio is defined[44]

$$\phi = \frac{[\mathrm{N}]_\mathrm{tot} L_{SV}}{[S]_\mathrm{tot} L_\mathrm{NV}}. \quad (4)$$

A flux ratio $\phi > 1$ means that vacancy sinks will be depleted in solute S, while $\phi < 1$ means that vacancy sinks will be enriched in solute S. From lattice site conservation, $J_V = -J_\mathrm{N} - J_S$ which implies $L_\mathrm{NV} = -L_{VV} - L_{SV}$. We assume local equilibrium between isolated V, isolated

S and VS pairs, thus $[VS] = [V][S]z_{VS}$. z_{VS} is the partition function of cluster VS, that is the sum of all microscopic configurations of the VS pair weighted by their Boltzmann factor with respect to isolated V and S[45]. Assuming $[\mathrm{N}]_{\mathrm{tot}} \simeq 1$ (valid for dilute solid solutions) and $[S]_{\mathrm{tot}} \simeq [S]$ (valid as long as the vacancy concentration is much lower than the impurity concentration), we rewrite ϕ in Eq. 4 in terms of cluster transport coefficients

$$\phi = \frac{-1}{[S]\left(1 + \frac{L_{VV}(VS)}{L_{SV}(VS)}\right) + \frac{M(V)}{z_{VS}L_{SV}(VS)}}. \quad (5)$$

The kinetic properties of VS pairs will be studied thoroughly in Sec III B, and drag ratio and flux ratio will be computed and discussed in Sec. III C.

III. RESULTS

A. Energetics of solutes near (001) surface and vacancies

1. *Incorporation energies*

We first study the incorporation energies of C and O on the N-sublattice of both UN bulk and UN(001) surface. Figure 1 shows the bulk structure and the various solute sites considered. Impurity atoms have been set in a substitutional position either located in an isolated or in two consecutive nitrogen sites. Incorporation energies define the relative stability of an element located in a pre-existing vacancy in the material. In the present work, Eq. 6 defines these incorporation energies and was used to obtain the values listed in Table I. In this equation, E_S corresponds to the total energy of a UN system where an impurity S is incorporated in a N-vacancy; E_V is the total energy of the UN system containing a N-vacancy; and E^S_{ref} is the total energy of the impurity atom in its reference state. In the present work, the reference states were the chemical potentials of C, N and O, in graphite, N_2 (g) and O_2 (g) states, respectively[46]. In this convention, the most stable state is the one having the most negative incorporation energy.

$$E_{\mathrm{inc}} = E_S - E_V - E^S_{\mathrm{ref}}. \quad (6)$$

The data in Table I shows that the vacancy formation and impurities incorporation energies found in the bulk and in the central layer of the surface structure are quite similar, showing that the slab is large enough to avoid interaction between the two surfaces of the slab. The formation of N-vacancies in the surface requires less energy compared with the bulk and this is in agreement with the qualitative argument that the nitrogen atom located in the surface has a reduced number of chemical bonds compared with bulk.

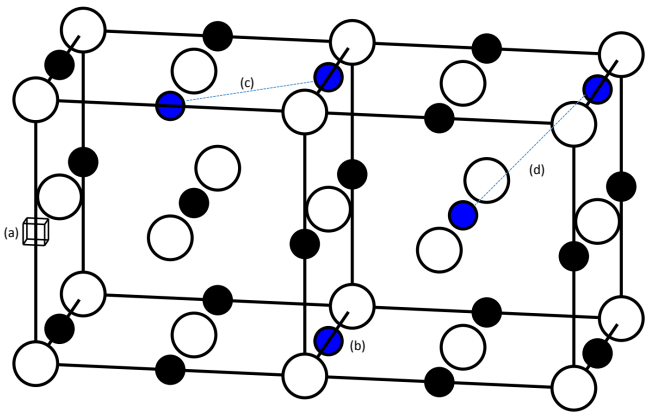

Figure 1. Bulk UN structure and the various defects considered in this study: N vacancy (a); isolated impurity in N position (b); impurities in two nearest neighbor N sites with same spin orientation (c) and and with opposed spin (d).

Table I. Incorporation energies (eV) of C and O impurities in UN bulk and UN(001) surface. Reference states used are the chemical potential of graphite, N_2 (g), and O_2 (g). Negative values indicate the energetically favorable incorporation. In the second column, "s" means same spin, "o" means opposed spin.

Defect		Bulk	Central layer of (001) slab	(001) surface
N_{vac}		+2.27	+2.30	+2.09
C_N		−3.22	−3.25	−3.05
O_N		−5.90	−5.88	−5.90
C_N-O_N 1NN	s	−8.90	−9.22	−8.79
	o	−8.89	−9.20	-
C_N-C_N 1NN	s	−6.25	−6.54	−5.94
	o	−6.49	−6.56	-
O_N-O_N 1NN	s	−11.68	−11.84	−11.59
	o	−11.78	−11.87	-

The incorporation of carbon and oxygen in the N-vacancy is energetically favorable in the bulk and in the (001) surface. Furthermore, the results reveal that the incorporation of impurities in the configuration when another impurity is in first nearest neighbor position (1NN, see Fig. 1c and d) has an energy which is higher than that of two isolated impurities. This is true for bulk and surface structures, and it shows that there is no thermodynamic driving force for impurity cluster formation. The only exception is the pair of C atoms in adjacent spin planes, which reduce the total energy of the system by 0.05 eV when they are 1NN to one another instead of being isolated. This value is small and beneath the convergence threshold of our ab initio calculations.

Moreover, it is found that all isolated defects have an energetic preference (up to 0.2 eV) to be located in the bulk rather than in the surface. Note that the isolated O impurity shows the same incorporation energy for bulk and surface. The energy difference between bulk and

surface can be larger for impurity pairs, but the bulk configuration is always energetically favored.

In order to get a better understanding of the electronic structure and bonding features of bulk and surface, charge density distributions were investigated. The results obtained for C and O in bulk and surface structures are shown in Fig. 2. From this analysis, we observe that C and O behave similarly in the bulk structure, that is they disturb 2 U atoms, cf. Fig. 2a and 2b. However, in the surface, the type of chemical bond formed for each of these impurities is different. The C atom is bound with 4 U atoms in the (001) plane (Fig. 2c), while the O atom is bound with 3 U atoms in the (001) plane (Fig. 2d), and a significant bonding charge can be seen halfway between O and U in the (001) plane (Fig 2f). Thus, the chemical coordination found for oxygen is different in the surface compared with the one in the bulk and for C in the surface. This result shows that the oxygen possess higher flexibility in types of chemical bond to be formed with U, i.e. it can bind with different bond angles, which seems not possible for C. Thus O may be more stable than C in the surface, which is in accordance with the incorporation energy obtained in Table I.

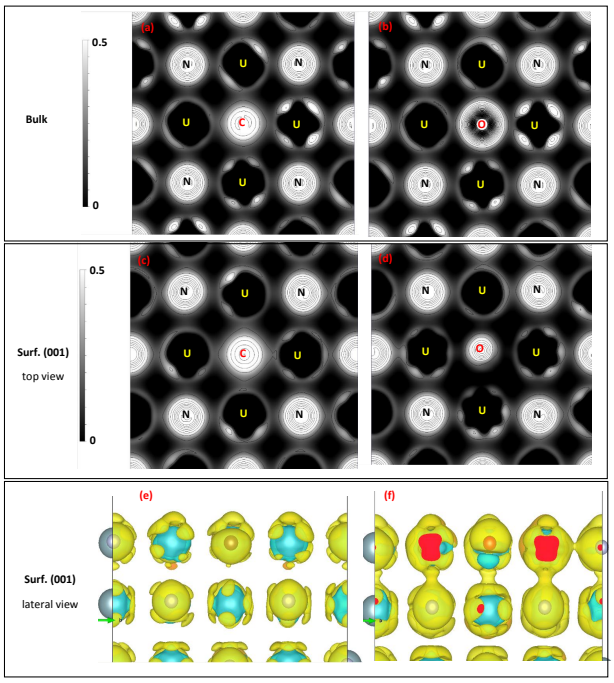

Figure 2. (a-d) Charge density difference (crystal density minus superposition of isolated atomic densities) of carbon and oxygen in UN bulk and (001) surface; (e-f) 3d view of the (100) cut. Blue and yellow colors represent charge accumulation and depletion, respectively. The isovalue is set to $\pm 0.03 \text{Å}^{-3}$.

Based on the above discussion, we found that there is no strong thermodynamic driving force for segregation of C and O impurities towards the surface, revealing that the surface segregation process in this material should be driven mainly by kinetic factors. Furthermore it is demonstrated that C and O have different chemical environments in the surface.

2. *Vacancy-solute binding energy*

We compute the binding energy of carbon and oxygen with a nitrogen vacancy in the UN structure. The binding energies were calculated using Eq. 7: E_{VS} (S=C,O) is the total energy of a system containing V and S close to one another and E_{bulk} is the energy of bulk UN. In this formulation, a positive binding energy indicates that the vacancy solute pair is more stable than isolated vacancy and solute.

$$E_{\text{bind}}\,(VS) = (E_V + E_S) - (E_{VS} + E_{\text{bulk}})\,. \qquad (7)$$

All the configurations considered are shown in Fig. 3 and the results are described in Table II. Symmetrically unique 1NN and 3NN configurations are distinguished as opposed spin "o" or same spin "s" configurations. Due to the crystal symmetry the 2NN and 4NN are always between sites with spins oriented in the same directions. However, these configurations can be either normal to the spin plane ("N" configuration) or tangential to the spin plane ("T" configuration) as a consequence of the magnetic orientation. To distinguish between these, we adopt the subscripts T or N.

As can be seen in Table II, the impurities interact with a N-vacancy in a non-monotonous way with respect to the $V - S$ distance, which can give rise to a complex motion of vacancies and solutes. It is noteworthy that in 1NN configuration, the VO interaction is more attractive than the VC interaction. On the other hand, when considering the 2NN position (in which there is a uranium atom between the impurity and vacancy) the attractive interaction with oxygen disappears. In this position, only carbon shows an attractive interaction with a N-vacancy. For both impurities, the interactions tend to go to zero beyond 4NN. The increase for 5NN is due to the limited size of the simulated structure which creates interactions with periodic images. These 5NN binding energy values are not considered fully trustworthy and will not be used in the subsequent modeling parts of this paper.

3. *Vacancy-solute migration energies*

From the relaxed structure configurations, we computed migration energies of all the possible vacancy jumps around the impurity starting from a 1NN or 2NN configuration. We considered only vacancy-assisted migration on the N sublattice because C and O are highly unstable in a U site[21]. Figure 4 shows schematically the considered atomic jumps and the specific nomenclature that we use. The obtained migration energies (E_{m}) are

Table II. Binding energies (eV) of carbon and oxygen with a N-vacancy in the UN structure.

Configuration	$E_{bind}\,(VC)$	$E_{bind}\,(VO)$
1NN same spin	-0.19	0.12
1NN opposed spin	0.10	0.26
2NN tangential	0.01	-0.10
2NN normal	0.07	-0.15
3NN same spin	0.12	0.29
3NN opposed spin	0.27	0.16
4NN tangential	0.01	0.09
4NN normal	-0.03	0.03
5NN same spin	0.06	0.16
5NN opposed spin	0.21	0.15

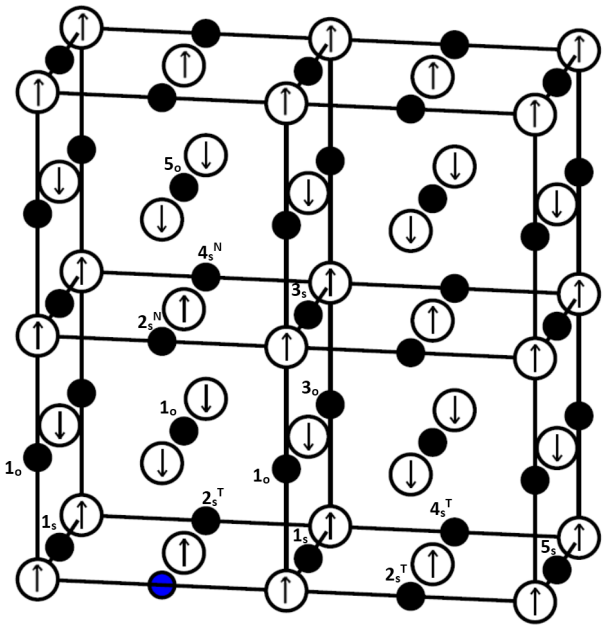

Figure 3. Nearest neighbor (NN) positions of the vacancy with respect to the solute (blue atom). "o" stands for opposite spins, "s" stands for same spin, "T" for tangential and "N" for normal. Black sphere represent the N-sublattice and open circles represent the U-sublattice.

listed in Table III. Saddle-point energies ($E_{\rm sp}$) are also presented in Table III, and are defined by Eq. 8. For a given jump sequence, the highest $E_{\rm sp}$ defines, as a first approximation, the rate limiting step for this specific migration path[47].

$$E_{\rm sp} = E_{\rm m} - E_{\rm bind}\,(VS)\,. \tag{8}$$

Table III shows that the solute-vacancy exchange migration energies are significantly lower for O than for C. This low value is a consequence of the path followed by O atom in the diffusion process as reported in previous work[21]. Consequently, we expect that vacancy exchanges more frequently with O atoms, but this is not conclusive to predict some drag phenomenon, nor that the long-range diffusion mechanism will be more efficient. The

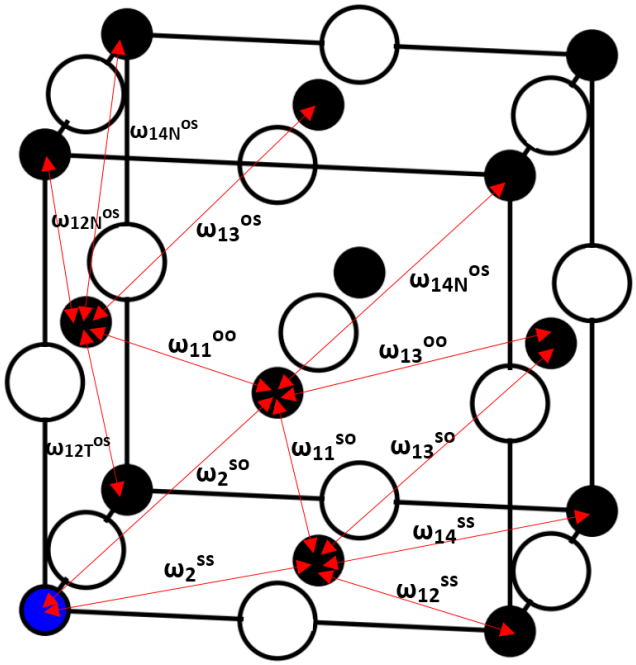

Figure 4. Schematics of the vacancy jumps around a solute considered in this study. The subscript represents the distance between V and S in the initial and final configurations. The superscript represents the spin orientation between the planes that contain V and S, both in the initial and final configurations.

atomic scale information from Table III must now be statistically averaged to obtain macroscopic kinetic coefficients, which will provide some insight into the diffusion mechanism of VS pairs (Sec. III B).

B. Solute diffusivities

Figure 5 shows the mobility contributions $M\,(V)$, $M\,(VC)$ or $M\,(VO)$ computed with the self-consistent mean field method, using as inputs the binding and migration energies from Table II and III. For each cluster V, VO and VC, two mobilities are shown; one corresponds to diffusion in the T-direction (tangential to spin planes, solid lines) and the other corresponds to diffusion in the N-direction (normal to spin planes, dashed lines).

Isolated vacancies have anisotropic jump rates in the bulk system (see Table III), and isolated V will preferentially jump in the N-direction (migration energy is 2.07 eV, compared with 2.23 eV in the T-direction). But jumps in the N-direction also have a component along the T-direction, meaning that successive jumps in the N-direction can produce long-range diffusion in the T-direction, and this is why both solid and dashed green lines in Fig. 5 have the same slope (i.e. same migration energy, cf. Table IV). Their slightly different prefactor stems from different kinetic correlations. So the same

Table III. Transition energies (eV) of carbon and oxygen in the UN structure. "Ini" correspond to the initial configuration of the VS pair and "Fin" to the final one. The number in parenthesis corresponds to the backward migration barrier. Transitions are represented in Fig. 4. The ω_2 transitions involve a displacement of the solute.

Ini	Fin	Label	E_{mig} (C)	E_{sp} (C)	E_{mig} (O)	E_{sp} (O)
1_{s}	1_{s}	ω_{2}^{ss}	2.72 (+0.00)	2.55	1.86 (+0.00)	1.69
1_{o}	1_{o}	ω_{2}^{so}	2.80 (+0.00)	2.48	2.01 (+0.00)	1.79
1_{o}	1_{o}	$\omega_{11}^{\mathrm{oo}}$	2.97 (+0.00)	2.87	2.38 (+0.00)	2.16
1_{s}	1_{o}	$\omega_{11}^{\mathrm{so}}$	2.43 (+0.12)	2.45	2.16 (+0.14)	2.02
1_{s}	2_{sT}	$\omega_{12\mathrm{T}}^{\mathrm{ss}}$	2.42 (+0.12)	2.44	2.59 (-0.22)	2.47
1_{o}	2_{sT}	$\omega_{12\mathrm{T}}^{\mathrm{os}}$	2.01 (+0.00)	1.91	2.58 (-0.36)	2.32
1_{o}	2_{sN}	$\omega_{12\mathrm{N}}^{\mathrm{os}}$	2.27 (-0.03)	2.17	2.12 (-0.41)	1.86
1_{s}	3_{o}	$\omega_{13}^{\mathrm{so}}$	2.37 (+0.29)	2.39	2.13 (+0.04)	2.01
1_{s}	3_{s}	$\omega_{13}^{\mathrm{ss}}$	2.54 (+0.02)	2.43	2.46 (+0.03)	2.20
1_{o}	3_{o}	$\omega_{13}^{\mathrm{oo}}$	2.67 (+0.17)	2.57	2.48 (-0.10)	2.22
1_{o}	4_{sT}	$\omega_{14\mathrm{T}}^{\mathrm{os}}$	2.23 (+0.03)	2.25	2.45 (-0.02)	2.33
1_{o}	4_{sN}	$\omega_{14\mathrm{N}}^{\mathrm{os}}$	2.15 (-0.13)	2.05	2.29 (-0.23)	2.03
2_{sN}	3_{s}	$\omega_{2\mathrm{N}3}^{\mathrm{ss}}$	2.88 (+0.05)	2.81	2.85 (+0.45)	2.33
2_{sT}	3_{o}	$\omega_{2\mathrm{T}3}^{\mathrm{so}}$	2.68 (+0.17)	2.58	2.23 (+0.26)	2.99
2_{sT}	5_{s}	$\omega_{2\mathrm{T}5}^{\mathrm{ss}}$	2.31 (-0.04)	2.21	2.46 (+0.30)	2.57
2_{sT}	5_{oT}	$\omega_{2\mathrm{T}5\mathrm{T}}^{\mathrm{so}}$	2.69 (+0.11)	2.59	2.34 (+0.26)	2.44
∞	∞	ω_{0}^{ss}	2.23 (+0.00)	2.23	2.23 (+0.00)	2.23
∞	∞	ω_{0}^{so}	2.07 (+0.00)	2.07	2.07 (+0.00)	2.07

mechanism will produce V diffusion in all directions, but this mechanism is more effective in the N-direction than it is in the T-direction. Table IV shows the results of fitting the mobilities in Fig. 5 to Arrhenius expressions

$$M(\alpha) = D_0 \exp\left(-\frac{E_{\mathrm{m}}}{k_{\mathrm{B}}T}\right). \tag{9}$$

It turns out that all VS mobilities do not follow Arrhenius laws on the full temperature interval. We chose $T = 600$ K as the approximate transition temperature between migration mechanisms, to have all mobilities fitted on the same temperature interval. Below (and above) this transition temperature, mobilities can be fitted to Arrhenius expressions. The fact that the effective migration energy changes between low and high temperatures indicates a change in the main migration mechanism for VS pairs.

For a given temperature range, VC pairs have similar migration energies along every diffusion direction, which shows that they are diffusing in every direction using the same atomic mechanism. As for the isolated vacancy, diffusion prefactors differ slightly, because a given mechanism is not necessarily equally effective in all directions. Upon increasing the temperature above 600 K, the effective migration energy of a VC pair decreases by 0.18 eV, which indicates that a mechanism that is less probable than the previous one is more efficient at generating long-range diffusion phenomena. It will thus become dominant at high temperatures where probability differences between various kinetic trajectories decrease.

Contrary to the two previous clusters (V and VC), VO pairs have a non-negligible diffusion anisotropy at low temperature, which diminishes as temperature increases. Also, diffusion in the T-direction is more efficient than in the N-direction. Again, the change in the effective migration energy as temperature increases is attributed to a change in the main paths leading to long-range diffusion. Note that the main path can in fact be a combination of various kinetic trajectories or migration mechanisms.

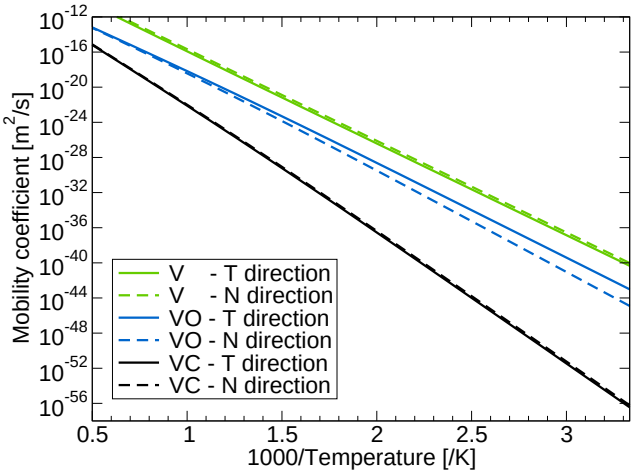

Figure 5. Mobility coefficients of cluster α (α being either an isolated vacancy V, a VO pair or a VN pair) as a function of the inverse temperature. For each cluster, there are two mobilities because diffusion is anisotropic. Mobilities in the T direction are shown as solid lines, while mobilities in the N direction are shown as dashed lines. Arrhenius fits of these curves in limited temperature ranges are provided in Table IV.

Table IV. Arrhenius fits to the mobility curves plotted in Fig. 5 for two temperature ranges: $T < 600$ K and $T > 600$ K. The variation of the diffusion prefactor and the migration energy between these fits points towards a change in diffusion mechanisms for VC and VO pairs.

		$T < 600$ K		$T > 600$ K	
		D_0 [m^2/s]	E_{m} [eV]	D_0 [m^2/s]	E_{m} [eV]
V	T-direction	4.00×10^{-6}	2.09	4.00×10^{-6}	2.09
	N-direction	5.83×10^{-6}	2.07	5.83×10^{-6}	2.07
VC	T-direction	1.84×10^{-7}	2.96	7.34×10^{-9}	2.79
	N-direction	2.21×10^{-7}	2.95	7.81×10^{-9}	2.77
VO	T-direction	8.57×10^{-8}	2.14	8.06×10^{-9}	2.01
	N-direction	3.62×10^{-7}	2.29	1.30×10^{-8}	2.11

Figure 6 shows the total (solid lines) and uncorrelated contributions (dashed lines) to the diagonal transport coefficients of the VO pair, $L_{\alpha\alpha}(V\mathrm{O})$ defined in Eq. 3, where $\alpha \in \{V, \mathrm{O}\}$. Because the solute requires a vacancy to move, it cannot dissociate from the pair by itself, meaning that $AD_{\mathrm{OO}}(V\mathrm{O}) = 0$ and $L_{\mathrm{OO}}(V\mathrm{O}) = M(V\mathrm{O})$. On the other hand, the association/dissociation contribution is non-zero for $\alpha = V$. The uncorrelated contribution is simply calculated as a

thermodynamic average of all possible atomic jump frequencies, while the complete calculation including kinetic correlations can be thought as a thermodynamic average of jump sequences (or trajectories). Thus, the ratio between these two relates to the efficiency of each individual jump and the probability that a given jump gets canceled out by subsequent jumps.

At low temperature, the uncorrelated contribution is similar for both coefficients $L_{VV}\,(VO)$ and $L_{OO}\,(VO)$, which indicates that the vacancy spends most of its time around the O atom. As temperature increases, the uncorrelated contribution to $L_{VV}\,(VO)$ becomes larger than the uncorrelated contribution to $L_{OO}\,(VO)$ because jumps where the vacancy dissociates (not very probable at low temperature) become more and more likely. Kinetic correlations arise because of either: 1. migration mechanisms and local lattice topology or 2. difference in the various possible jump rates from an initial state. The former does not evolve with temperature, while the latter always decreases with temperature. For this reason, kinetic correlations have less and less effect as temperature increases. It is thus expected that the total transport coefficients and the uncorrelated contributions converge towards similar values at high temperature. Nevertheless, it requires much higher temperatures (compared with $L_{VV}\,(VO)$) for the $L_{OO}\,(VO) = M\,(VO)$ to be unaffected by kinetic correlations other than the ones coming from the geometry of the lattice (i.e. when all migration energies are identical). As a summary, Fig. 6 shows that at low temperature V and O migrate mostly together, forming a pair. As temperature increases, V is able to dissociate more easily from the O atom, hence its migration path are more efficient (i.e. uncorrelated).

Correlations effects are discussed for the kinetic properties of VO pairs in the T-direction only because they show similar features in the N-direction. On the other hand, diagonal transport coefficients for VC pairs show very small kinetic correlations, which is why they are not shown here.

We now combine the data from Table III and Figs. 5 and 6 to get a more precise idea of atomic-scale migration mechanisms. We will focus on low temperature migration paths, because then it is reasonable to assume that there is a single trajectory that controls the kinetic properties of the system. As the temperature increases, differences in trajectory probabilities decrease and several migration paths might have similar impact on the overall kinetic properties. When a single trajectory controls the kinetic properties, the effective migration energy can be estimated using the highest barrier approximation[47]. This approximation states that the effective migration barrier is the energy difference between the most energetic saddle-point and the most stable state of this trajectory. This simple estimation does not take into account kinetic correlation, but it can be compared with migration energies from Table IV to make sure that the correct migration mechanism of VS pairs has been identified. Our procedure is the following: we start from a

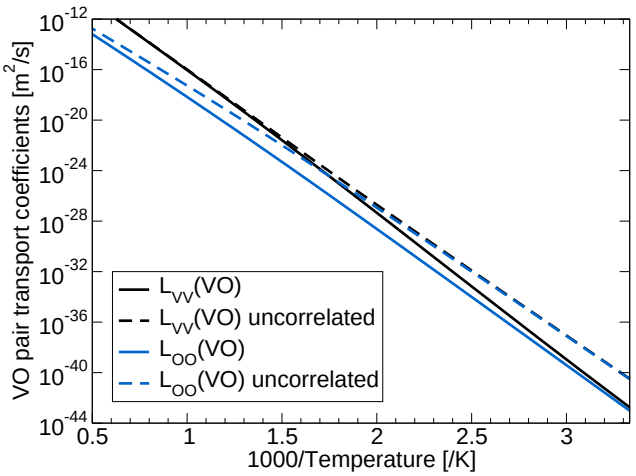

Figure 6. Diagonal transport coefficients of VO pairs, $L_{VV}\,(VO)$ and $L_{OO}\,(VO)$ (solid black and blue lines, respectively). The uncorrelated contributions are given as dashed lines. Both transport coefficients are identical at low temperature, while kinetic correlations for the $L_{VV}\,(VO)$ coefficient are significantly reduced as temperature increases (compared with $L_{OO}\,(VO)$). This behavior hints towards a change in the migration mechanism as temperature increases, as pointed out in Table IV.

vacancy-solute exchange, required to produce any motion of solutes. Then, we look for the lowest saddle-point jump from this configuration and try to construct a path using only this kind of jumps, and such that the final configuration is a translation (along the diffusion direction) of the initial one.

Figure 7 shows the identified low-temperature migration mechanisms of VO pairs. There are two possible vacancy-oxygen exchange jumps with similar migration energies (1.74 eV and 1.75 eV) so both of these could be a starting point. Among all vacancy jumps around the solute, the lowest saddle-point is found for $\omega_{12\mathrm{N^{os}}}$ (1.86 eV). To perform this jump, V and O need to be in adjacent spin planes (1NN "o" configuration), so out-of-plane V-O exchange is required. Then the $\omega_{12\mathrm{N^{os}}}$ jump brings the vacancy in the 2NN "N" configuration, from which it can jump back to another 1NN "o" configuration. This configuration allows a new exchange with the solute and leads to long range diffusion. This mechanism for diffusion in the T-direction is shown on the left-hand side of Fig. 7. To make sure that we identified the correct mechanism, the associated migration barrier is estimated as $E_\mathrm{m} = 1.86 + 0.26 = 2.12$ eV, in good agreement with the 2.14 eV from Table IV. For this system, it is interesting to note that diffusion in the T-direction is more efficient using V-S exchange perpendicular to spin planes.

A similar method is applied to identify the VO migration mechanism in the N-direction, depicted on the right-hand side of Fig. 7. This mechanism only goes through 1NN configurations ("o" and "s") and the effective migration energy is $E_\mathrm{m} = 2.02 + 0.26 = 2.28$ eV, again in

good agreement with the 2.29 eV obtained from fitting the mobility coefficient (see Table IV). Yet, there are various jumps with similar saddle-point energies: $\omega_{11^{os}}$ (2.02 eV), $\omega_{13^{so}}$ (2.01 eV) and $\omega_{14n^{os}}$ (2.03 eV). This means that at some point during the migration path, the vacancy has equal chances to keep moving around the solute or diffuse away from it. These dissociation jumps are represented by green arrows (5' and 6'). Thus, long range diffusion in the N-direction is less efficient.

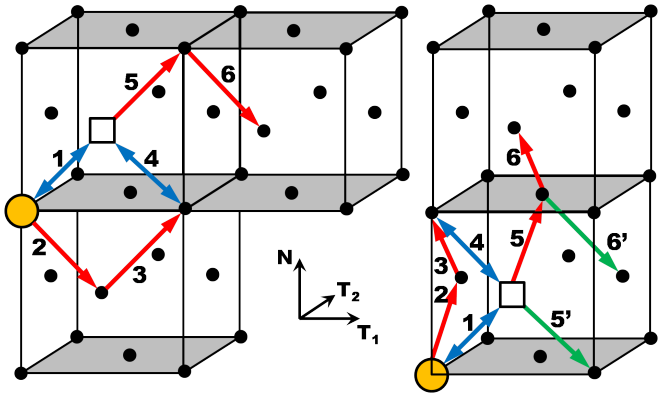

Figure 7. Long-range diffusion mechanism for VO pairs. Left-hand side plot shows diffusion in one of the T-directions, and right-hand side plot shows diffusion in the N-direction. The initial position of the solute and the vacancy are depicted as a yellow sphere and white square, respectively. Host N atoms are represented by small black spheres, while host U atoms are not shown. Blue double-headed arrows denote an exchange between S and V, while red single-headed arrows denote an exchange V and host U atoms. The number besides each arrow corresponds to the order in which these jumps proceed. The final position of the solute is obtained by following double-headed arrows, while the final position of the vacancy is at the sixth arrow head. Final and initial position are thus equivalent. For the right-hand side plots, additional green arrows denote possible dissociation path, where jumps 5' and 5" have a probability similar to jump 5.

The same tools are used to understand the diffusion of VC pairs at the atomic scale. The migration mechanism identified for VO migration in the T-direction is also valid for VC diffusion in the same direction, and rotating the trajectory by 90 degrees gives the most probable mechanism in the N-direction. In the case of C, the same migration mechanism accounts for diffusion in all directions because the limiting step is the vacancy-carbon exchange, and the effective migration energy is $E_{\mathrm{m}} = 2.70 + 0.27 = 2.97$ eV, in agreement with results from Table IV. The limiting step being the V-C exchange, the uniqueness of the migration path is not guaranteed, even at low temperature, because the vacancy is able to perform a large number of jumps around the solute in between two exchanges with the solute. Still, the mechanism shown on the left-hand side of Fig. 8 is the most probable trajectory of V around the carbon atom. This mechanism only leads to diffusion in the N-direction, and the rotated mechanism leading to diffusion in the T-direction has a lower probability. Diffusion in the T-direction is thus tricky to understand. On the right-hand side of Fig. 8, jump 2 will probably not lead to long-range migration because the following lowest barrier jump (labeled 3) leads to the stable 3NN "o" configuration, from which the complex easily dissociates. The same argument applies for the $(1, 2', 3')$ sequence. Jump 2" would lead to long range migration of the VC pair in the T-direction, but it is much less probable than the aforementioned trajectories. Thus, in the T-direction, the VC cluster is expected to diffuse via successive association and dissociation jumps, rather than as a pair that stays bound all the time. Note that the probability of V and C forming a pair rather than being isolated is given by the VC binding energy and does not depend on the migration mechanism. Therefore at equilibrium, the fact that C diffuses by successive associations and dissociations with V does not necessarily means that it will diffuse slowly.

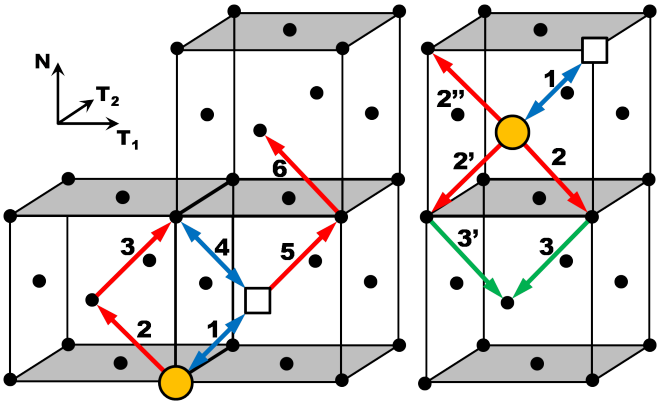

Figure 8. Long-range diffusion mechanism for VC pairs. The left-hand side plot shows diffusion in the N-direction, and the right-hand side plot shows diffusion in one of the T-directions. Symbols and colors have the same signification as in Fig. 7. For the right-hand side plots, additional green arrows denote possible dissociation path. Trajectories $(1, 2, 3)$ and $(1, 2', 3')$ are more probable than trajectory $(1, 2'')$, which implies that after a V-C exchange, V will more easily migrate away from C rather than around it.

C. Radiation-induced segregation

This section discusses the radiation-induced segregation properties of VC and VO pairs as Sec. III A has shown that there is no thermodynamic driving force for isolated impurity surface segregation. Figure 9 presents the VS pair drag ratio, which controls the qualitative nature of the flux coupling phenomenon, for VO (blue lines) and VC (black lines) pairs in both T-direction (solid lines) and N-direction (dashed lines). The VO pairs flux ratio is positive at low temperature, which is consistent with the mechanisms presented in Fig. 7, where the most probable migration path is the one where the vacancy diffuses in the first two NN shell around the solute, and

exchanges with the solute, leading to long-range diffusion of the pair cluster as a whole. We already explained that it should be easier to dissociate a VO pair diffusing in the N-direction than one diffusing in the T-direction. This comment is in agreement with the fact that the drag ratio is always lower in the N-direction (dashed blue line) compared with the T-direction (solid blue line). As temperature increases, jump sequences leading to cluster dissociation become more and more probable, thus the drag ratio decreases, and becomes negative at some point. This is expected because in the infinite temperature limit, all rates become equal and the drag ratio is given by

$$\lim_{T\to\infty} \frac{L_{SV}\left(VS\right)}{L_{SS}\left(VS\right)} = -\frac{1}{f_0} \simeq -1.28, \tag{10}$$

where f_0 is the self-diffusion correlation factor for face centered cubic systems.

VC pair diffusion in the N-direction behaves similarly as VO pairs, which is not surprising as the predominant migration path in this direction is similar to the VO migration path in the T-direction (cf. Fig. 8 left plot). Most striking is the VC drag ratio in the T-direction (solid black line) which is always negative from room temperature up. The drag ratio shows a minimum around $T \simeq 1300$ K. This negative drag ratio is most probably related to the fact that it is difficult for the VC pair to diffuse in the T-direction without dissociating, as shown in Fig. 8. It is thus expected that an isolated vacancy will encounter a solute and exchange with it. After this jump, the vacancy can either start a jump sequence which will lead to solute diffusion in the N-direction, or dissociate from the solute, both with equal probabilities. The first possibility does not lead (on average) to any diffusion in the T-direction. In the second possibility, the vacancy will have performed a single exchange with the solute (in this process V and S flow in opposite directions) and then dissociates. Successive encounters of this type lead to a net flux of solutes in a direction opposite to that of the vacancy flux, hence the negative drag ratio. It is also interesting to note that VC pairs show very small anisotropy in the mobility coefficient (cf. Fig. 5), yet they show qualitatively opposite flux coupling properties between the T-direction and the N-direction.

The drag ratio explains how vacancy and impurity flux are related to each other but it is not sufficient to understand the radiation-induced segregation phenomenon. To this end, we need to compute the flux ratio ϕ between impurity and matrix atoms, as defined in Eq. 4. Figure 10 shows this flux ratio computed for C and O in the $T-$ and $N-$ directions, and for two solute concentrations: $[S] = 10^{-6}$ and $[S] = 10^{-3}$. Note that below a certain solute concentration threshold, ϕ does not depend on solute concentration anymore. The results obtained at $[S] = 10^{-6}$ correspond to such dilute system. At low temperature, vacancies drag oxygen atoms, leading to O enrichment at point defect sinks. At $T \simeq 800$ K or $T \simeq 1000$ K depending on the diffusion direction, the drag ratio becomes negative, which is related to the inverse Kirkendall phenomena. Nevertheless, the flux of V to sinks still creates O enrichment up to $T \simeq 1100$ K because of the relative probability of V to exchange with a matrix atom rather than an impurity atom. In a dilute system (typically $[O] = 10^{-6}$), we predict O depletion at higher temperatures. As the O concentration increases in the system, higher temperatures are required to observe solute depletion, and for $[O] = 10^{-3}$, our model predicts only O enrichment up to 2000 K. Flux ratio in the V-C system are about 2-3 orders of magnitude lower than in the V-O system such that C segregation at sinks is expected to be small. Whatever the diffusion direction and the C concentration, our model always predicts C enrichment at sinks, even though the flux coupling behavior of VC pairs is qualitatively different in $T-$ and $N-$directions (cf. Fig. 9).

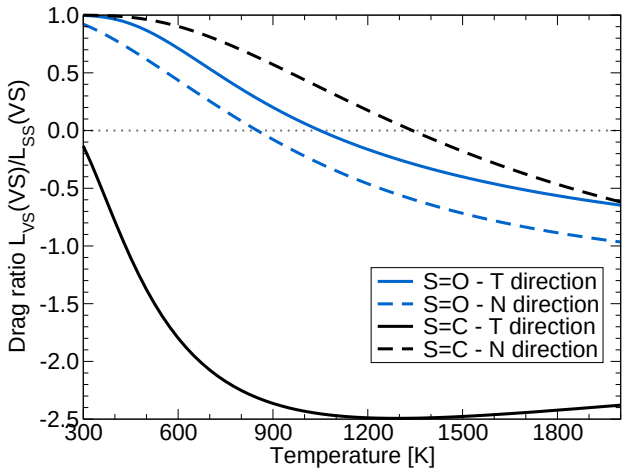

Figure 9. Drag ratio $L_{VS}\left(VS\right)/L_{SS}\left(VS\right)$ of vacancy-solute pairs (VS, $S \in \{C, O\}$) as a function of temperature. Drag ratio for VO pairs (resp. VC pairs) are shown in blue (resp. black) for both T-direction (tangential to spin planes, solid lines) and N-direction (normal to spin planes, dashed lines). The vastly different drag ratio coefficients indicate that V migrates differently around a C atom or around an O atom.

D. Comparison with experiments

To the best of our knowledge, there is only one experimental measurement of N self-diffusion in UN[48]. The N self-diffusion coefficient follows the Arrhenius law in the 2050-2270 K temperature interval, with a diffusion prefactor equal to 5×10^{-10} m^2.s^{-1} and an activation energy equal to 1.88 eV. According to the authors of this study, their UN sample was non-stoichiometric with a ratio U/N=0.996. Assuming that all the non-stoichiometry is due to the existence of vacancies on the N sublattice, the vacancy concentration is estimated to be 4×10^{-3}. With

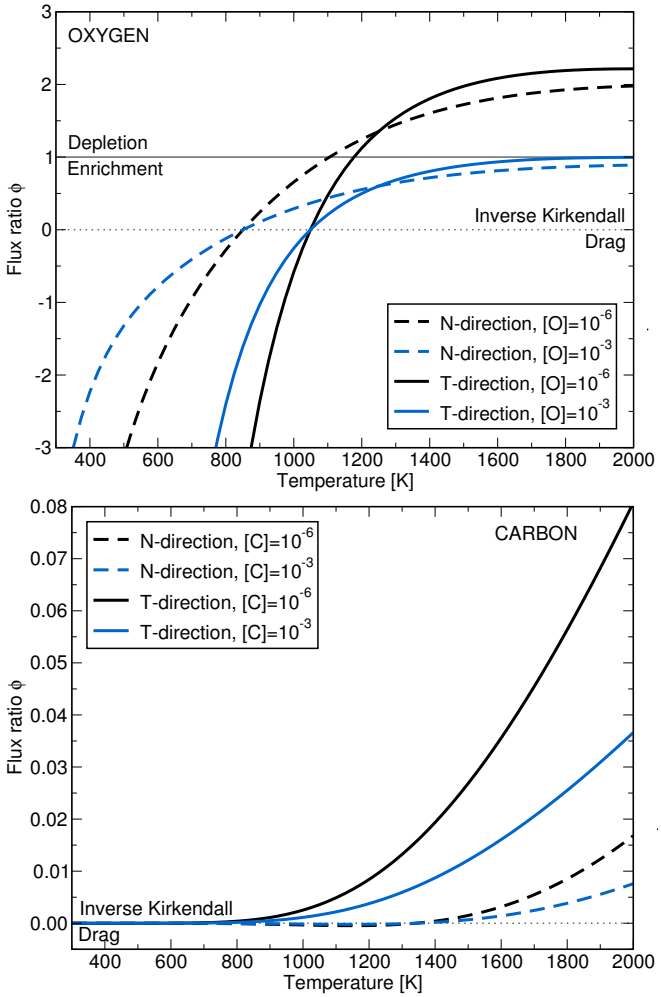

Figure 10. Flux ratio ϕ (Eq. 4) for O (top) and C (bottom) impurities in UN as a function of temperature. Dashed lines and solid lines correspond to the flux ratio in the $N-$ and $T-$ directions, respectively. Colors relate to impurity concentration.

such vacancy concentration our calculations combining DFT and SCMF allow us to compute the following Arrhenius parameters for N self-diffusivity : diffusion prefactor 2×10^{-8} m^2.s^{-1} and activation energy 2.08 eV. In the experimental temperature range (2050-2270 K), our calculation overestimates the experimental measurement by 1 order of magnitude, while it underestimates the extrapolation from experimental data below 1170 K. The agreement is quite good considering the numerous assumptions that have been made : DFT provides T = 0 K energies while experimental diffusivity measurements were performed above 2050 K; we neglected variations in attempt frequencies between different vacancy jumps; we assumed all vacancies to be isolated without any interactions between them; the vacancy concentration, to which N diffusivity is proportional, is bluntly taken as the reported deviation from stoichiometry; at such high temperatures UN is not anti-ferromagnetic anymore; there are no other measurements of N self-diffusivity to confirm the experimental measures. More experimental data is obviously needed to test the predictive power of the methodology presented in this paper. In order to acquire this data, our calculations can readily be used to estimate temperature ranges and time scales where N, C or O diffusion in UN can be measured.

IV. CONCLUSIONS

In this study, we combine DFT+U+OMC calculations and the SCMF method to investigate the thermodynamic and transport properties of C and O in UN. Incorporation energies computed with DFT show that C and O are both thermodynamically favored in the bulk rather than in the UN(001) surface. The formation of impurity pairs is thermodynamically unfavorable, both in the bulk and in the surface. We compute VS (S=C,O) binding energies up to 4NN configurations, which show non-monotonic evolutions with the V-S distance. Migration barriers between all of these configurations are also computed and inform the SCMF method to evaluate cluster transport coefficients. Arrhenius fits to cluster mobilities combined with the highest barrier approximation allows us to identify the main migration mechanism of each species. The O atoms bind with vacancies, and the pair diffuses as a whole in $T-$ and $N-$ directions. The same mechanism applies for C diffusion in the $N-$direction, while C diffusion in the $T-$direction occurs via successive associations and dissociations. This translates into an anisotropic flux coupling behavior of C with V below 1300 K: the drag ratio is negative in the $T-$direction, and positive in the $N-$direction. On the contrary, the VO drag ratios are similar in all directions (positive up to $\simeq$1000 K). As for the analysis of flux ratios, our calculations predict that C should segregate to vacancy sinks under irradiation, even though the magnitude of this radiation-induced segregation should be small. The O impurities behave similarly at high enough concentration ([O] $> 10^{-3}$), except that the magnitude of the segregation phenomenon should be much higher. If the O concentration is lower than this value, we predict an oxygen depletion at vacancy sinks for temperatures above 1100 K.

ACKNOWLEDGMENTS

The authors acknowledge support from the UIUC-KTH collaboration project INSPIRE. The authors gratefully acknowledge discussions with Maylise Nastar, Luca Messina, Dallas Trinkle and Pascal Bellon about the SCMF method. Work by TS was supported by the U.S. Department of Energy (DOE), Office of Science, Basic Energy Sciences (BES) under Award DE-FG02-05ER46217. Michel Freyss' help on the OMC scheme was very important for the completion of this article, and we are grateful to him, Emerson Vathonne and Marjorie

Bertolus at CEA/DE, and Boris Dorado at CEA/DAM for the implementation of this method in VASP. Funding from Svensk Kärnbränslehantering AB is acknowledged. The computations were performed on resources provided by the Swedish National Infrastructure for Computing (SNIC) at PDC and NSC.

* Corresponding author; tschul@illinois.edu

[1] H. Matzke, *Science of advanced LMFBR fuels : solid state physics, chemistry, and technology of carbides, nitrides, and carbonitrides of uranium and plutonium*, edited by H. Matzke (North Holland, Amsterdam, 1986).

[2] P. Wilson, ed., *The Nuclear Fuel Cycle* (Oxford University Press, 1996).

[3] F. Goldner, in *Enhanced Accident Tolerant LWR Fuels National Metrics Workshop, Germantown, MD* (2012).

[4] G. Youinou and R. Sen, Nuclear Technology **188**, 123 (2014).

[5] S. Hayes, J. Thomas, and K. Peddicord, Journal of Nuclear Materials **171**, 289 (1990).

[6] M. Allbutt and R. Dell, Journal of Nuclear Materials **24**, 1 (1967).

[7] B. Rogozkin, N. Stepennova, Y. Fedorov, M. Shishkov, F. Kryukov, S. Kuzmin, O. Nikitin, A. Belyaeva, and L. Zabudko, Journal of Nuclear Materials **440**, 445 (2013).

[8] R. Metroka, *Fabrication of Uranium Mononitride Compacts, NASA Technical Note TN-5876*, Tech. Rep. (NASA, July 1970).

[9] L. des Irradiations, *Carbon-14 production and nitrogen-15 enrichment of nitride fuels*, Tech. Rep. (CEA, 2001).

[10] A. G. Vakhtin, V. D. Dmitriev, and S. N. Ermolaev, *Experience in operating fuel elements in a nitride core of a BR-10 reactor*, Tech. Rep. (Report at a Soviet-French Seminar, Obninsk, 1992).

[11] B. D. Rogozkin, N. M. Stepennova, and A. A. Proshkin, Atomic Energy **95**, 624 (2003).

[12] P. Modak and A. K. Verma, Physical Review B **84**, 024108 (2011).

[13] D. Gryaznov, E. Heifets, and E. Kotomin, Physical Chemistry Chemical Physics **14**, 4482 (2012).

[14] T. Bo, J.-H. Lan, Y.-J. Zhang, Y.-L. Zhao, C.-H. He, Z.-F. Chai, and W.-Q. Shi, Phys. Chem. Chem. Phys. **18**, 13255 (2016).

[15] D. Bocharov, D. Gryaznov, Y. Zhukovskii, and E. Kotomin, Surface Science **605**, 396 (2011).

[16] D. Bocharov, D. Gryaznov, Y. Zhukovskii, and E. Kotomin, Journal of Nuclear Materials **435**, 102 (2013).

[17] A. Liechtenstein, V. Anisimov, and J. Zaanen, Physical Review B **52**, R5467 (1995).

[18] B. Meredig, A. Thompson, H. A. Hansen, C. Wolverton, and A. van de Walle, Physical Review B **82**, 195128 (2010).

[19] A. Claisse, M. Klipfel, N. Lindbom, M. Freyss, and P. Olsson, Journal of Nuclear Materials **478**, 119 (2016).

[20] G. Jomard, B. Amadon, F. Bottin, and M. Torrent, Physical Review B **78**, 075125 (2008).

[21] D. A. Lopes, A. Claisse, and P. Olsson, Journal of Nuclear Materials **478**, 112 (2016).

[22] M. Nastar, V. Y. Dobretsov, and G. Martin, Philosophical Magazine A **80**, 155 (2000).

[23] M. Nastar, Philosophical Magazine **85**, 3767 (2005).

[24] V. Barbe and M. Nastar, Philosophical Magazine **87**, 1649 (2007).

[25] T. Garnier, V. R. Manga, D. R. Trinkle, M. Nastar, and P. Bellon, Phys. Rev. B **88**, 134108 (2013).

[26] M. Nastar, Phys. Rev. B **90**, 144101 (2014).

[27] T. Schuler and M. Nastar, Physical Review B **93**, 224101 (2016).

[28] L. Messina, M. Nastar, N. Sandberg, and P. Olsson, Physical Review B **93**, 184302 (2016).

[29] G. Kresse and J. Hafner, Physical Review B **47**, 558 (1993).

[30] G. Kresse and J. Hafner, Journal of Physics: Condensed Matter **6**, 8245 (1994).

[31] G. Kresse and J. Hafner, Physical Review B **49**, 14251 (1994).

[32] J. P. Perdew, K. Burke, and M. Ernzerhof, Physical review letters **77**, 3865 (1996).

[33] Y. Lu, B.-T. Wang, R.-W. Li, H.-L. Shi, and P. Zhang, Journal of Nuclear Materials **410**, 46 (2011).

[34] P. W. Tasker, Journal of Physics C: Solid State Physics **12**, 4977 (1979).

[35] H. J. Monkhorst and J. D. Pack, Physical Review B **13**, 5188 (1976).

[36] G. Mills, H. Jónsson, and G. K. Schenter, Surface Science **324**, 305 (1995).

[37] H. Jónsson, G. Mills, and K. W. Jacobsen, (1998).

[38] C. Varvenne, F. Bruneval, M.-C. Marinica, and E. Clouet, Phys. Rev. B **88**, 134102 (2013).

[39] H. Wu, T. Mayeshiba, and D. Morgan, Sci. Data **3**, 160054 (2016).

[40] V. Baranov, Y. N. Devyatko, A. Tenishev, A. Khlunov, and O. Khomyakov, Journal of Nuclear Materials **434**, 248 (2013).

[41] H. B. Callen, *Thermodynamics and an Introduction to Thermostatistics, 2nd Edition*, edited by J. W. . Sons (Wiley, 1985).

[42] A. Claisse, T. Schuler, D. A. Lopes, and P. Olsson, Physical Review B **94**, 174302 (2016).

[43] M. Nastar and F. Soisson, Comprehensive Nuclear Materials , 471 (2012).

[44] L. Messina, M. Nastar, T. Garnier, C. Domain, and P. Olsson, Phys. Rev. B **90**, 104203 (2014).

[45] C. Barouh, T. Schuler, C.-C. Fu, and M. Nastar, Phys. Rev. B **90**, 054112 (2014).

[46] G. Aylward and T. Findlay, *SI Chemical Data* (J. Wiley, 1974).

[47] C. Barouh, T. Schuler, C.-C. Fu, and T. Jourdan, Physical Review B **92**, 104102 (2015).

[48] J. Holt and M. Almassy, J. Am. Ceram. Soc. **52** (1969).